*Sensors and Materials*, Vol. 31, No. 10 (2019) 3007–3022
MYU Tokyo



S & M 1988

# Magnetic Scattering in Ni Wires Fabricated on Ferroelectric $LiNbO_3$ Substrate for Magnetic Sensor Application

Ryo Nakamura,[1,3] Shunya Saegusa,[1,3] Satoru Suzuki,[1] Aiko Nakao,[1] Yuichi Utsumi,[1] Takuo Ohkochi,[2,3] Masaki Oura,[3] Yukako Takizawa,[4] Tsunemasa Saiki,[4] Taekhyeon Lee,[5] Kab-Jin Kim,[5] Keisuke Yamada,[6] Takeshi Ogasawara,[7] and Akinobu Yamaguchi[1,3*]

[1]Laboratory of Advanced Science and Technology for Industry, University of Hyogo, 3-1-2 Kouto, Kamigori, Hyogo 678-1205, Japan
[2]Japan Synchrotron Radiation Research Institute, 1-1-1 Kouto, Sayo, Hyogo 679-5198, Japan
[3]RIKEN SPring-8 Center, 1-1-1 Kouto, Sayo, Hyogo 679-5148, Japan
[4]Manufacturing Technology Department, Hyogo Prefectural Institute of Technology, 3-1-12 Yukihira, Suma, Kobe, Hyogo 654-0037, Japan
[5]Department of Physics, Korea Advanced Institute of Science and Technology, Daejeon 34141, Republic of Korea
[6]Department of Chemistry and Biomolecular Science, Faculty of Engineering, Gifu University, 1-1 Yanagido, Gifu City, Gifu 501-1193, Japan
[7]Electronics and Photonics Research Institute, National Institute of Advanced Industrial Science and Technology, Tsukuba, Ibaraki 305-8565, Japan

(Received June 28, 2019; accepted September 30, 2019)

***Keywords:*** magnetoresistance, heterojunction, magnetic domain structure, spin-dependent scattering, multiferroic functional materials

We investigated the magnetoresistive property of a micrometer-scale Ni wire with a uniaxial magnetic anisotropy induced by the formation of a heterojunction between a Ni layer and a single-crystal lithium niobate ($LiNbO_3$) substrate. We revealed that the domain structure can be controlled by adjusting the wire alignment and that its magnetoresistance (MR) is dependent on the magnetic domain structure as well as the reversal process. The introduction of a heterojunction is a crucial method of controlling the magnetic domain structure owing to the additional generation of the magnetic anisotropy. This control of the magnetic domain structure is very useful for investigating the fundamental physical mechanism and producing artificial multiferroic functional materials and devices. The relatively large MR response observed in transport measurements alludes to the possibility that the spin-dependent scattering mechanism occurs in the domain and domain wall.

## 1. Introduction

The control of the domain structure, domain wall propagation, and magnetization reversal is at the heart of magnetism; exchange interaction, crystalline anisotropy, demagnetizing field control due to shape, exchange bias, and magnetostriction work to direct the magnetization along the respective preferred directions and maintain balance among them, resulting in the magnetic domain structure being formed to minimize the total energy of the system. In

*Corresponding author: e-mail: yamaguti@lasti.u-hyogo.ac.jp
https://doi.org/10.18494/SAM.2019.2494

ISSN 0914-4935 
https://myukk.org/

nanomagnetism and spintronics, this control of magnetism is of interest because they are strongly associated with not only the fundamental magnetism but also magnetic device applications. For example, nonvolatile magnetic random accesses memory and microwave oscillators are expected to be developed as next-generation devices. In a confined artificial magnet, a disciplined magnetic domain structure and magnetization switching properties can be achieved to some extent by nano/microfabrication.[1–8] In such an artificial magnet, lateral and vertical confinement often leads to special states, such as vortex[9–13] and antivortex domain configurations,[14] which can be achieved using a strong magnetic shape anisotropy. The exchange bias and magnetostriction also offer key techniques to control the magnetic domain structure and its reversal characteristics.[15–22] The magnetization dynamics in these systems have been studied by various techniques including time-resolved X-ray magnetic circular dichroism-photoemission electron microscopy (XMCD-PEEM),[23–25] Kerr microscopy,[26,27] Brillouin light scattering (BLS),[28,29] and electrical detection techniques.[3,5,13,22,30–34]

Recently, attempts to fabricate artificial multiferroic materials with their functionalities above room temperature have been focused on because the control of magnetic domain structures and their magnetization dynamics using electric fields or strain that is electrically induced through the piezoelectric effect has the potential to decrease the power consumption of devices from the viewpoint of constituent materials.[35] One idea to create a novel multiferroic material is given by introducing the concept of artificially fabricating a heterojunction composed of ferromagnetic and ferroelectric materials. In previous studies,[36,37] the piezoelectric effect was demonstrated to modulate magnetic characteristics through the magnetoelastic effect or magnetostriction. The competition between the shape magnetic anisotropy and the uniaxial magnetic anisotropy induced by the heterojunction results in the formation of a specific magnetic domain structure and the modulation of magnetization switching properties.[23,24] For example, a stripe domain structure in a Ni wire whose longitudinal axis was perpendicular to the *X*-axis of a lithium niobate ($LiNbO_3$) substrate was spontaneously formed in the near absence of a magnetic field, whereas a single-domain state was formed in a Ni wire aligned parallel to the *X*-axis direction of the $LiNbO_3$ substrate. Thus, this finding may provide a clue to developing novel artificial multiferroic materials with their functionalities above room temperature. Before the integration of artificial multiferroic materials, the magnetic properties associated with the heterojunction should be unveiled to take advantage of the development of applications such as domain wall logic and magnetic sensors.

The heterojunction leads to a specific spin texture through the formation of domain walls in a stripe domain structure. Recently, the Dzyaloshinskii–Moriya interaction (DMI)[38,39] at the interface has attracted much attention because it facilitates the stabilization of homochiral Néel domain walls.[40] Thus, a domain wall is not only a unique object but also plays a significant role in magnetization reversal and scattering properties. Here, we investigated the fundamental properties of the domains and domain walls formed in the Ni wire fabricated on the single-crystal lithium niobate ($LiNbO_3$) Y-cut 128° substrate. In particular, we present a physical interpretation of the magnetoresistance (MR) of Ni wires with the stripe domain structure. The role of the physical origin of the MR in the interpretation of our experiments is discussed in detail.

## 2. Materials and Methods

Ni micrometer-scale wires of 30 nm thickness were fabricated on a Y-cut 128° $LiNbO_3$ substrate by an electron-beam lithography and lift-off process with magnetron sputtering. After the formation of Ni wires, the wires were coated with a resist for electrode formation and baked at 100 °C for 3 min using a hot plate in air ambient. Separately from the microfabrication, 25-nm-thick Ni continuous films deposited on $SiO_2$/Si and Y-cut 128° $LiNbO_3$ substrates were prepared to evaluate their magnetization characteristics using a vibrating sample magnetometer (VSM: VSM-C7-10A, Toei Industry Co., Ltd., Tokyo). Figures 1(a)–1(c) show the magnetization curves of the Ni films deposited on various substrates, namely, (a) $SiO_2$/Si, (b) $LiNbO_3$ as-deposited, and (c) $LiNbO_3$ baked at 100 °C for 3 min using a hot plate, respectively, to confirm whether that the baking treatment contributes to magnetism. As shown in Fig. 1(a), the magnetization curves are almost independent of the magnetic field direction. In contrast to Fig. 1(a), the magnetization curves in Figs. 1(b) and 1(c) depend on the magnetic field direction, enabling us to adequately recognize the existence of easy and hard magnetization axes. These

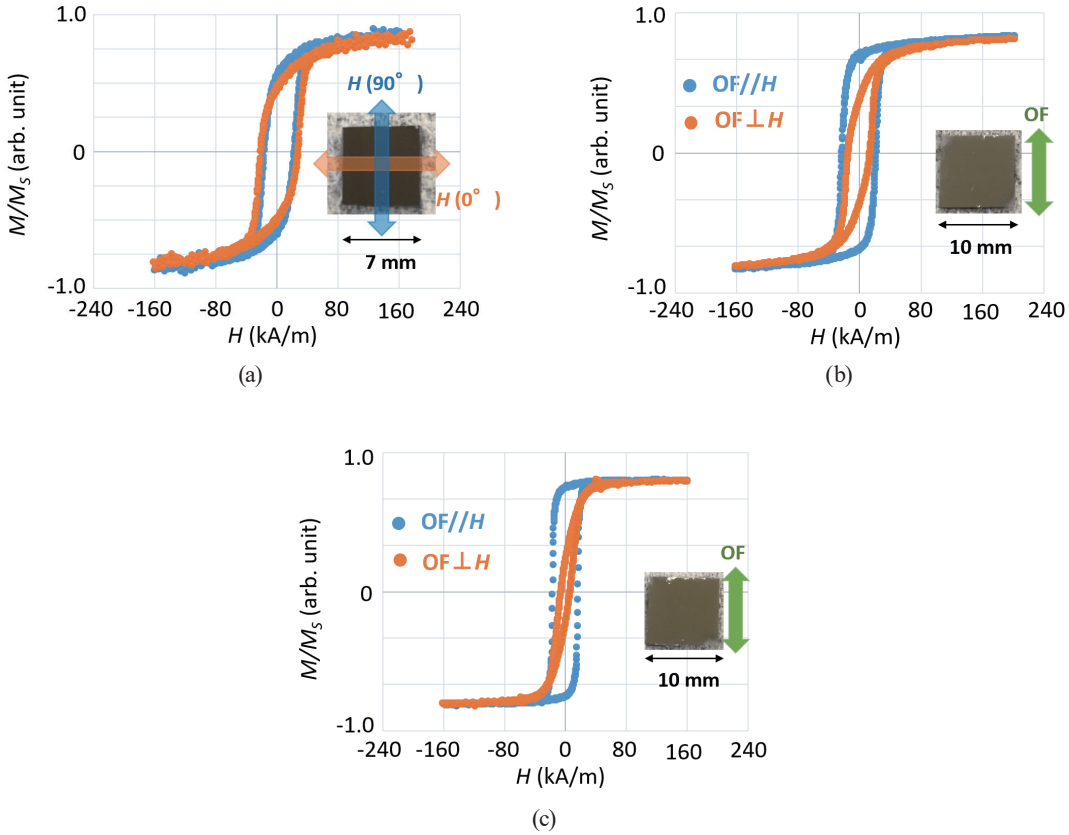


Fig. 1. (Color online) Magnetization hysteresis loops measured using vibrating magnetometer with 25-nm-thick Ni film deposited on (a) $SiO_2$/Si and (b) and (c) Y-cut 128° $LiNbO_3$ substrates. All the Ni films were covered with a 1-nm-thick Au capping layer to prevent oxidization. Only sample (c) was baked at 100 °C by using a hot plate in air ambient. The magnetic fields are applied parallel and perpendicular to the orientation flat (OF) direction of the $LiNbO_3$ substrate.

results indicate that the uniaxial magnetic anisotropy in the Ni films deposited on the $LiNbO_3$ substrate can be simultaneously induced.

By taking advantage of the uniaxial magnetic anisotropy induced from the substrate, we controlled the magnetic domain structure and magnetization reversal properties. Next, we measured the wire width dependence of the MR. Figure 2(a) shows a typical schematic of the MR measurement setup and system consisting of Ni wires and electrodes for the MR measurement. A Ni wire is placed in the aperture between the conductive strip lines of the coplanar waveguide (CPW) consisting of Cr (5 nm)/Au (80 nm). The wires prepared between the CPW strip lines are $w$ = 700 nm, 1 μm, 2 μm, 3 μm, and 5 μm in width and 100 μm in length as shown in Fig. 2. Furthermore, we investigated the wire width dependence of the MR.

The ground-signal-ground (GSG)-type microwave probe is connected to the CPW electrode, and the MR is measured by the lock-in detection technique. The external magnetic field is additionally applied in the substrate at tilting angles of $\theta$ = 0 and 90° from the longitudinal axis of the wire aligned perpendicular and parallel to the orientation flat (OF) direction of the $LiNbO_3$ substrate. The OF direction is parallel to the $X$-axis direction of the $LiNbO_3$ substrate.

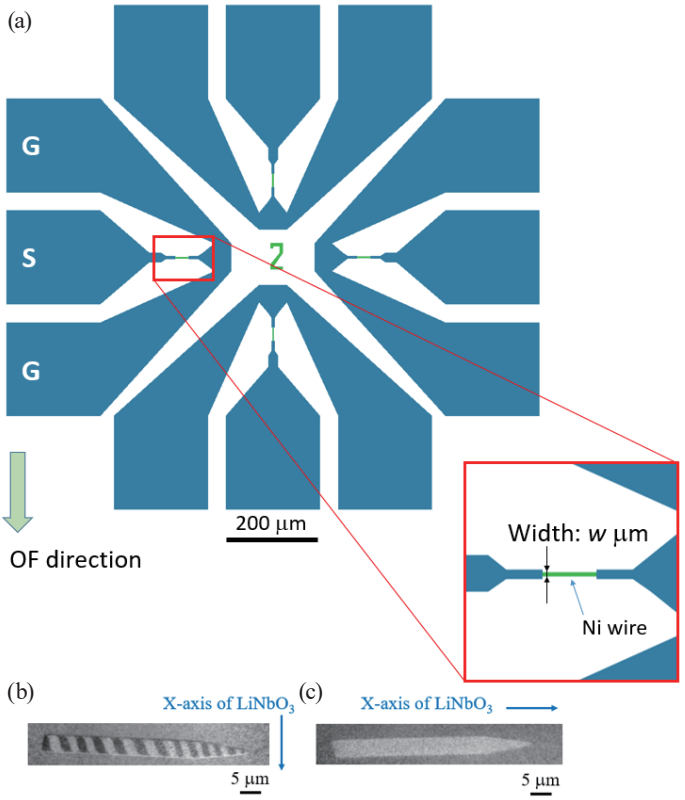


Fig. 2. (Color online) (a) Schematic of the MR measurement setup. The Ni wire is placed in the aperture between the conductive strip lines of the CPW consisting of Cr/Au. The GSG-type microwave probe is connected to the CPW and the MR is measured by the lock-in amplifier detection technique. The electrode gap is 30 μm. Typical XMCD-PEEM images of the Ni wires aligned (b) perpendicular and (c) parallel to the OF direction.

In this study, we prepared the systems in which the Ni wires were allocated perpendicular and parallel to the OF direction. We also focused on the basic magnetic response with respect to the field applied parallel or perpendicular to the Ni wire. All these experimental measurements were performed at room temperature.

## 3. Results and Discussion

In our previous study using XMCD-PEEM at the BL17SU and BL25SU beamlines of SPring-8,[23–25] the stripe domain and single-domain structures can be formed in the micrometer-scale Ni wires aligned perpendicular and parallel to the OF direction of the $LiNbO_3$ substrate, respectively. Figures 2(b) and 2(c) show the typical XMCD-PEEM images of stripe domain and single-domain structures in the Ni wires aligned perpendicular and parallel to the OF direction of the $LiNbO_3$ substrate, respectively. The length of the Ni wire is 30 μm. To investigate the magnetization reversal process, we measured the MR. Figure 3 shows the typical resistivity measurement results of the 700-nm-wide Ni wire when the magnetic fields were applied parallel and perpendicular to the longitudinal axis of the wire. Here, the Ni wire was directed perpendicular to the OF direction. In the MR measurements using the CPW electrode connected to the GSG probe, it is difficult to completely remove artifact effects associated with the contact resistance because of quasi four-probe measurement using the lock-in detection and prober system. Therefore, the absolute value of resistivity is not completely correct. In this study, we evaluated the MR ratio in the following. Figure 4 shows the MR ratio measurement results as a function of an external magnetic field applied parallel and perpendicular to the Ni wires with widths of 700 nm, 2 μm, and 5 μm in plane. Here, the MR ratio is defined as MR ratio (%) = $[R(H) - R(H_0)] / R(H_0) \times 100$, where $R(H)$ and $R(H_0)$ denote

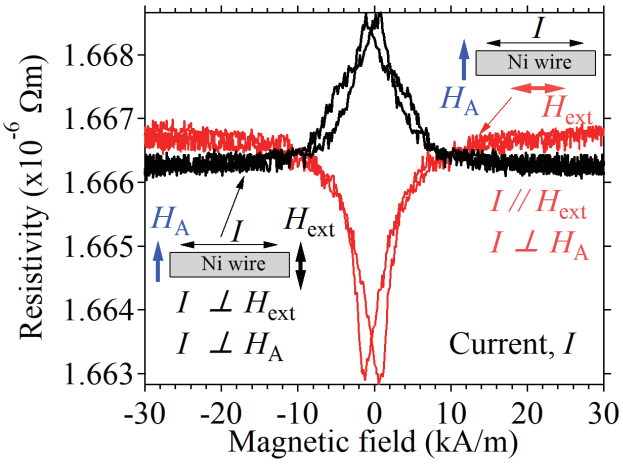


Fig. 3. (Color online) Resistivity of Ni wire aligned perpendicular to the uniaxial magnetic anisotropy induced by the heterojunction as a function of magnetic field applied parallel or perpendicular to the wire. The width of the wire is 700 nm.

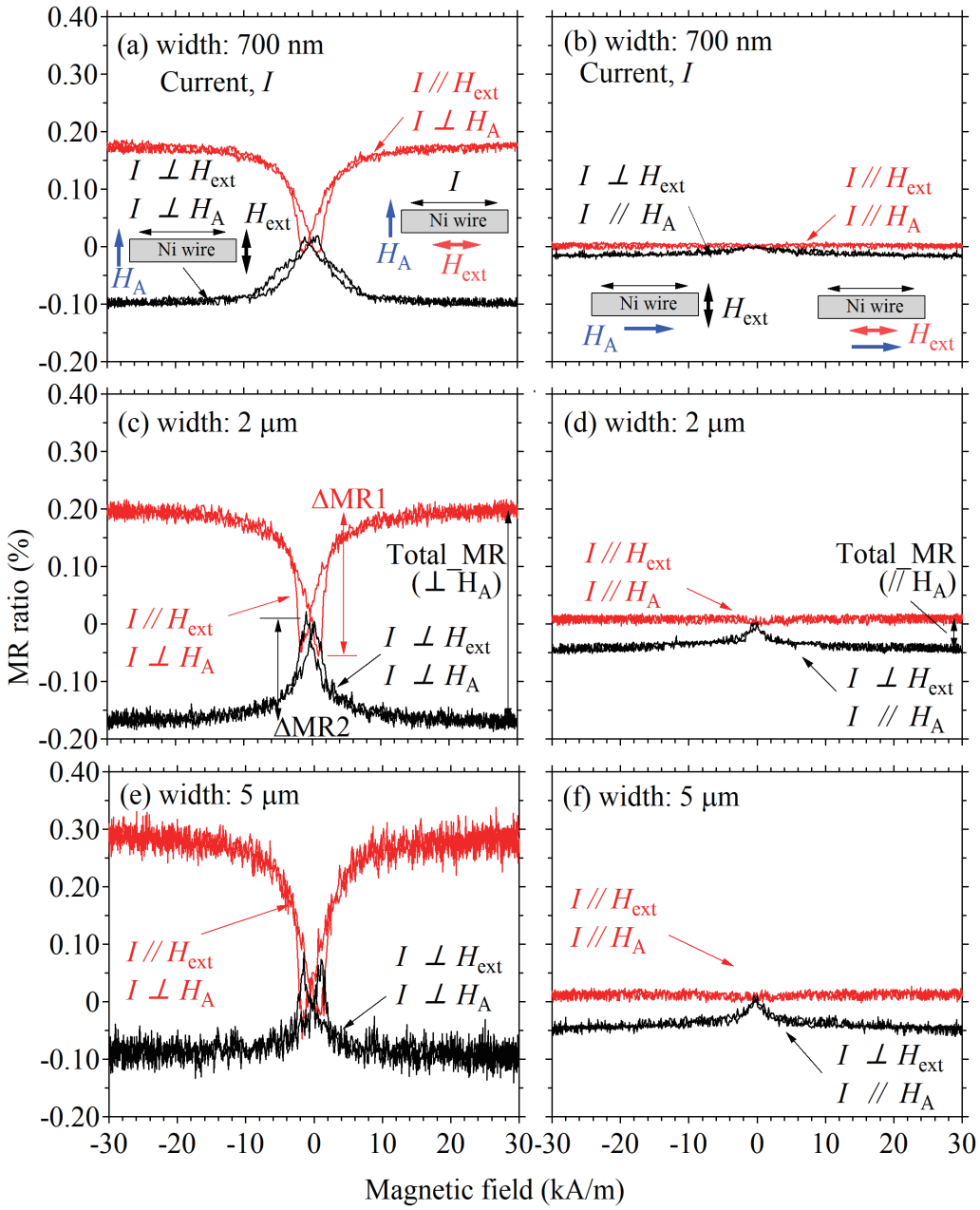


Fig. 4. (Color online) MR ratio as a function of the strength of the external magnetic field, $H_{ext}$, applied parallel and perpendicular to the longitudinal axis of the Ni wires with widths of (a, b) 700 nm, (c, d) 2 μm, and (e, f) 5 μm. The electric current $I$ flows along the wires. The Ni wires are aligned parallel and perpendicular to the uniaxial magnetic anisotropic field $H_A$. There are four combinations for the MR ratio measurements: [1] $I \parallel H_{ext}$ & $I \perp H_A$, [2] $I \perp H_{ext}$ & $I \perp H_A$, [3] $I \perp H_{ext}$ & $I \parallel H_A$, and [4] $I \parallel H_{ext}$ & $I \parallel H_A$.

the MRs at the applied magnetic fields of $H$ and $H_0$, respectively. Here, $H_0 = 0$. The red and black lines correspond to the MR ratio curves measured when the magnetic fields were applied parallel and perpendicular to the Ni wire, respectively. As is well known, when the magnetic field exceeded the coercive force, the MR was observed to be almost independent of the applied

magnetic field except the forcing effect. Below the coercive force, the MR varies with $(\cos\theta)^2$, where $\theta$ is the angle between the magnetization and the electric current. The MR behaviors are well known as the anisotropic MR (AMR) effect. The increase and decrease in MR ratio correspond to the increase in magnetization component directed parallel and perpendicular to the electric current *I,* respectively. Therefore, when the magnetic field ($H_{ext}$) is applied parallel to the Ni wire aligned perpendicular to the OF direction of the $LiNbO_3$ substrate (*X*-axis of $LiNbO_3$ crystal) in Fig. 4(a) (corresponding to the red MR curve, $I \parallel H_{ext}$ & $I \perp H_A$), the MR ratio is minimum near zero magnetic field, indicating that stripe domain structures are formed. Here, $H_A$ is the uniaxial magnetic anisotropy induced by the heterojunction and directed along the OF direction. The MR ratio is maximum in the near absence of a magnetic field when the magnetic field was applied perpendicular to the Ni wire, as shown in Fig. 4(a) (corresponding to the black MR curve, $I \perp H_{ext}$ & $I \perp H_A$). In this case, when the magnetization is saturated by a strong external magnetic field and directed to the external magnetic field perpendicular to the wire, the MR is low. With decreasing external magnetic field, the stripe domain is formed, and the magnetization component parallel to the electric current increases, resulting in the increase in MR. In the near absence of the external magnetic field, the stripe domain structure is expected to be spontaneously formed by the competition between the magnetic shape anisotropy and the magnetic anisotropy induced by the heterojunction in the Ni wire aligned perpendicular to the *X*-axis of the $LiNbO_3$ substrate. In contrast, when the Ni wire was aligned parallel to the OF direction, the MR ratio behaviors shown in Fig. 4(b) are very different from the results shown in Fig. 4(a). This difference is attributed to the fact that the single-domain structure is formed in the Ni wire aligned parallel to the OF direction of the substrate. The MR ratio behaviors shown in Fig. 4(b) can be understood using the typical magnetization reversal model with rotation magnetization and domain wall displacement.

To understand the magnetization reversal properties of the stripe domain and single-domain structures, micromagnetic simulation is performed.[41] Here, we analyzed a 30-nm-thick Ni wire with unit cells (size: $8 \times 8 \times 30$ nm$^3$). To clarify the magnetic basic behaviors of the system with the competition between the shape magnetic anisotropy and the uniaxial magnetic anisotropy induced by the heterojunction, the calculation model of 5 μm length and 1 μm width is systematically used to shorten the time for the calculation by understanding the physics. The material parameters of Ni, namely, the saturation magnetization $M_s$ of 0.6 T and the exchange stiffness constant A of $0.5 \times 10^{-11}$ J/m, are adopted in this study. We assumed that the magnetic anisotropy derived from the heterojunction between the Ni wire and the $LiNbO_3$ substrate was $K_u$ = 5.7 kJ/m$^3$. We set the Gilbert damping constant $\alpha$ = 0.01, 0.1, and 1. The basic physical mechanism and magnetic properties in the system can be semiquantitatively evaluated, although differing in detail.

We calculated the four alignments corresponding to the experimental MR measurement alignments. Figures 5(a) and 5(b) show the magnetization reversal processes of the stripe domain structure formed at zero magnetic field in the Ni wire aligned perpendicular to the uniaxial magnetic anisotropy when the external magnetic fields are swept parallel (case [1]) and perpendicular (case [2]) to the longitudinal axis of the Ni wire, respectively. The magnetic field dependences of magnetization components are also shown. These results can quantitatively

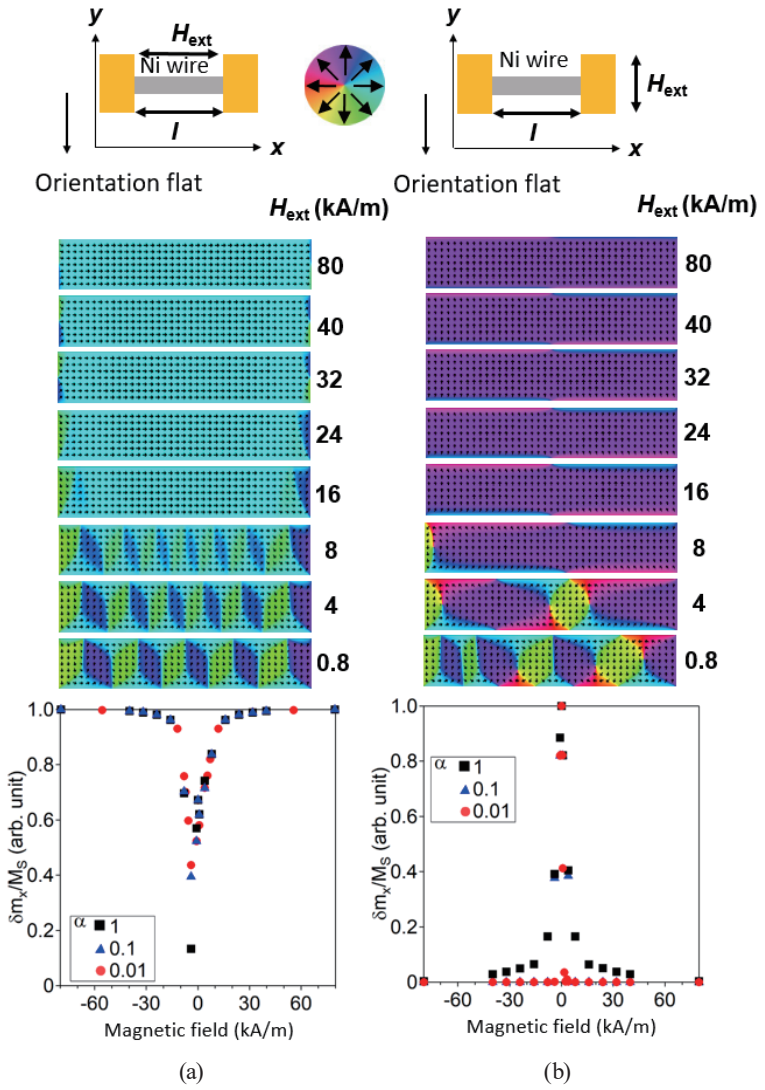


Fig. 5. (Color online) Schematic illustrations of the micromagnetic simulation setup in the cases (a) [1] $I \parallel H_{ext}$ & $I \perp H_A$ and (b) [2] $I \perp H_{ext}$ & $I \perp H_A$. A uniaxial magnetic anisotropic field, $H_A$, is induced along the OF direction. The OF direction is parallel to the $X$-axis of the $LiNbO_3$ substrate. The calculated magnetization distributions at magnetic fields of 0.8, 4, 8, 16, 24, 32, 40, and 80 kA/m are shown. The rainbow color indicates the in-plane component of magnetization. The summed perpendicular magnetization component $m_x$ is shown as a function of the applied magnetic field under the assumed damping constants of $\alpha$ = 0.01, 0.1, and 1.

explain the MR behaviors. In a similar way, Figs. 6(a) and 6(b) show the simulation results obtained when the Ni wire is aligned parallel to the uniaxial magnetic anisotropy (cases [4] and [3]). As a result, all the demonstrated micromagnetic simulation results are in qualitatively good agreement with the experimental results.

As described in our previous studies,[23,24] the comparison of MRs shown in Fig. 4 reveals that each saturation field is almost independent of the wire width. We reconfirm that the uniaxial magnetic anisotropy is derived from the heterojunction. Next, we examine whether

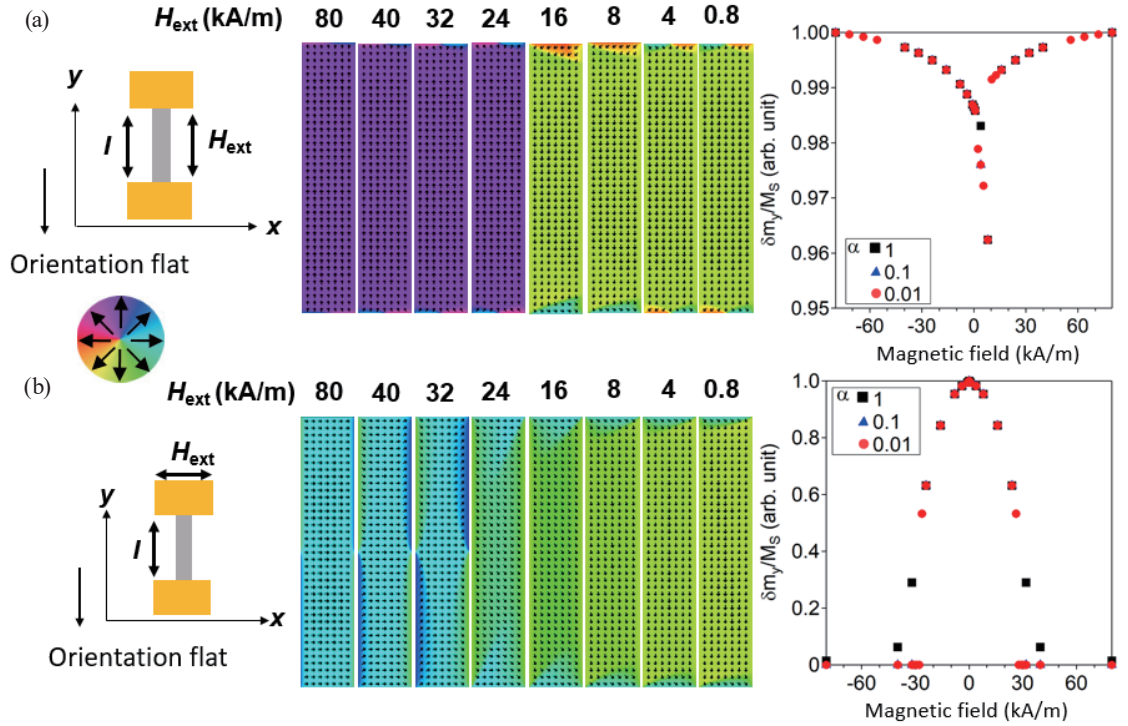


Fig. 6. (Color online) Schematic illustrations of the micromagnetic simulation setup in the cases (a) [4] $I \parallel H_{ext}$ & $I \parallel H_A$ and (b) [3] $I \perp H_{ext}$ & $I \parallel H_A$. A uniaxial magnetic anisotropic field, $H_A$, is induced along the OF direction. The OF direction is parallel to the *X*-axis of the $LiNbO_3$ substrate. The calculated magnetization distributions at magnetic fields of 0.8, 4, 8, 16, 24, 32, 40, and 80 kA/m are shown. The rainbow color indicates the in-plane component of magnetization. The summed perpendicular magnetization component $\delta m_y/M_s$ is shown as a function of the applied magnetic field under the assumed damping constants of $\alpha$ = 0.01, 0.1, and 1.

the MR ratio is dependent on the wire width. Here, we define the difference in MR ratio, $\Delta MR$ ratio, as $\Delta MR$ ratio (%) = $[|MR(H_R) - MR(H_{SAT})|]$, where MR($H_R$) is the MR obtained at the magnetic field $H_R$. In typical cases, $MR(H_R)$ is maximum or minimum in the near absence of the magnetic field $H_R$, while $MR(H_{SAT})$ becomes constant in the case of application of a sufficient magnetic field $H_{SAT}$ enough to saturate the magnetization. The value is strongly dependent on the angle between the magnetization and the electric current *I*. This MR change is basically derived from the AMR effect. Here, $MR(H_0)$ is defined as the MR in the absence of a magnetic field, $H_0 \sim 0$ kA/m. The estimated $\Delta MR$ ratios (%) of the 4 cases are as follows: [case 1: $\Delta MR1$] $I \parallel H_{ext}$ & $I \perp H_A$, [case 2: $\Delta MR2$] $I \perp H_{ext}$ & $I \perp H_A$, [case 3: $\Delta MR3$] $I \parallel H_{ext}$ & $I \parallel H_A$, and [case 4: $\Delta MR4$] $I \perp H_{ext}$ & $I \parallel H_A$, where *I* is the electric current flowing in the Ni wire. $H_{ext}$ and $H_A$ are respectively the external magnetic field and the uniaxial magnetic anisotropy field, which is induced parallel to the *X*-axis of the $LiNbO_3$ substrate. Moreover, we define 'Total $\Delta MR(\perp H_A)$' and 'Total $\Delta MR(\parallel H_A)$' as the maximum differences in MR ratio obtained by subtracting the MR ratios at which the magnetization is directed parallel and perpendicular to the electric current *I*, respectively. Here, 'Total

$\Delta MR(\perp H_A)$' and 'Total $\Delta MR(\| H_A)$' are obtained when the uniaxial magnetic anisotropy is directed perpendicular and parallel to the longitudinal axis of the Ni wire, respectively. 'Total $\Delta MR(\| H_A)$' is nearly equal to ΔMR4. The evaluated values of Δ*MR* and Total Δ*MR* are summarized in Fig. 7. In all the cases, the Δ*MR* ratios tend to saturate after increasing with the wire width. We found a clear anisotropic behavior: the Δ*MR* ratio is strongly dependent on the direction of the uniaxial magnetic anisotropy induced by the heterojunction. This is attributed to the fact that the resistance change is significantly affected by the domain structure and scattering process.

In particular, note that the magnetization component differences shown in Figs. 5(a), 5(b), and 6(b) are the same. The AMR differences in the cases of Figs. 5(a), 5(b), and 6(b) are expected to be the same; however, the experimental results are not consistent with the behaviors anticipated from the micromagnetic simulation results. These results indicate that the spin-dependent scattering derived from the stripe domain structure and domain walls contribute to the MR behaviors shown in Figs. 3 and 4. Therefore, the study on the heterojunction between ferromagnetic and ferroelectric materials provides clues to understanding the fundamental physics induced by the interface and controlling the magnetic domain structure, pinning, switching, and anisotropy, resulting in the modulation of the electric and magnetic responses of the devices.

Next, we reconsider the MR ratio change. The MR, $R(H) = \rho(H)L/S$, where $\rho(H)$, $L$, and $S$ are the resistivity when the external magnetic field $H$ is applied, length, and cross-sectional area of the wire, respectively. Therefore, the MR ratio should be independent of the wire dimensions. The relationship is given by MR ratio (%) = $[\rho(H) - \rho(H_0)] / \rho(H_0) \times 100\%$. The

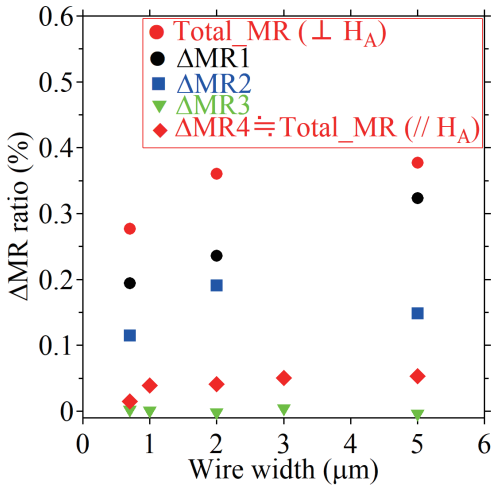


Fig. 7. (Color online) Wire width dependence of MR ratio differences, Δ*MR* ratio. [Δ*MR*1] $I \| H_{ext}$ & $I \perp H_A$, [Δ*MR*2] $I \perp H_{ext}$ & $I \perp H_A$, [Δ*MR*3] $I \| H_{ext}$ & $I \| H_A$, and [Δ*MR*4] $I \perp H_{ext}$ & $I \| H_A$, where $I$ is the electric current flowing in the Ni wire. 'Total $\Delta MR(\perp H_A)$' and 'Total $\Delta MR(\| H_A)$' as the maximum differences in MR ratio obtained by subtracting MR ratios at which the magnetization is directed parallel and perpendicular to the electric current, respectively.

$\Delta MR$ ratio (%), which is defined as the difference between the maximum and minimum MR ratios, should also be independent of the wire dimensions. In fact, as shown in Fig. 7, the $\Delta MR$ ratio (%) increases with the wire width in all the cases. Before discussing this behavior, we observe that the $\Delta MR$ ratio (%) of the case [$\Delta MR4$] seems to saturate as the wire width increases. The AMR of the single-domain state is expected to contribute to the saturation value. To simplify the observed phenomena, we assume that the stripe domain structure consists of series-connected single domains and domain walls as shown in Fig. 8. Then, we define that the $\Delta MR \text{ ratio}(\%) = n \times \Delta MR4 + (n-1) \times R_{DW} \sim n \times (\Delta MR4 + R_{DW})$, where $n$ is the number of single domains directed perpendicular to the longitudinal axis of the wire and $R_{DW}$ is the resistance derived from the domain wall. This approximation is the series resistance circuit model. In addition, we approximate that $R_{DW}$ is sufficiently smaller than $\Delta MR4$. As a result, here, we approximately calculate $n$ as $n$~$\Delta MR$ ratio (%) / $\Delta MR4$.

In this study, we also assume that the MR ratio is independent of the direction of the uniaxial magnetic anisotropy from the heterojunction for simplicity. We should consider that the stripe domain structures and their resistivities obtained at the remaining state do not completely match in the absence of the magnetic field as shown in Figs. 4 and 5. On the basis of the prerequisite, we estimate the number of domains $n$ by dividing 'Total $\Delta MR(\perp H_A)$', $\Delta MR1$, and $\Delta MR2$ by $\Delta MR4$ as shown in Fig. 9.

In our previous studies,[23,24] the domain widths estimated using the XCMD-PEEM images are well known to be in good agreement with those calculated by the micromagnetic simulation. This result indicates that the domain width is almost proportional to the wire width and that the domain size is about 75% of the wire width.[23,24] In this study, the electrode gap $L$ is 30 μm, and the domain size can be estimated. Then, the number of domains in the remaining state can be evaluated as $n \sim L / (0.75w)$. The fitting curve is drawn as the red solid line in Fig. 9. The

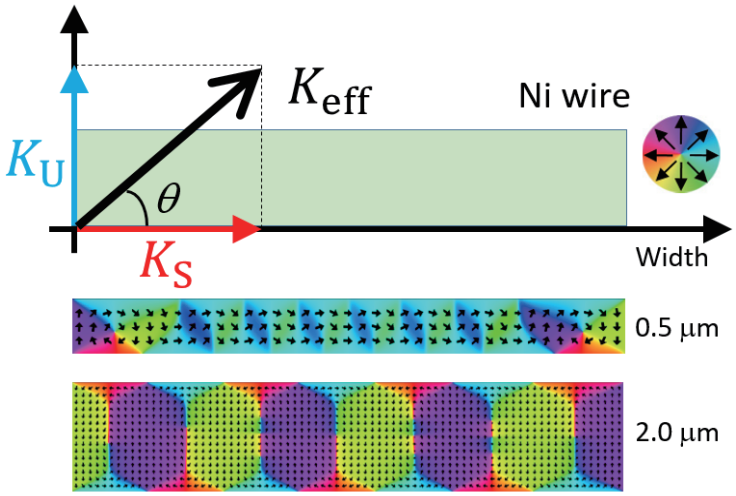


Fig. 8. (Color online) Schematic image of the coordinate system in the Ni wire. The domain structures of 0.5- and 2.0-μm wide Ni wires were calculated by micromagnetic simulation.

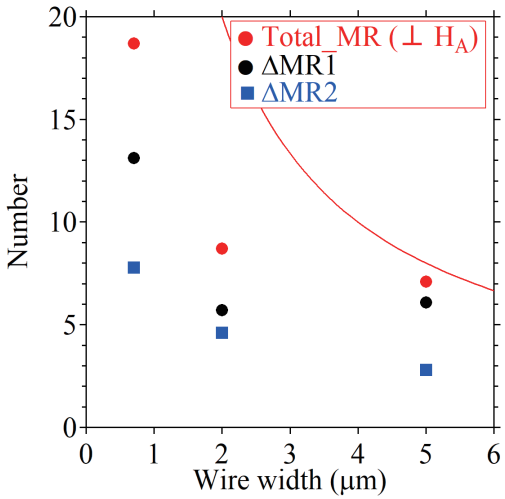


Fig. 9. (Color online) Wire width dependence of MR ratio differences, Δ*MR* ratio.

trend agrees with the experimental results. However, as the width decreases, the disagreement becomes larger. This result indicates that either the numerator is small or the denominator Δ*MR*4 is large. Δ*MR*4 is the total AMR difference from the single-domain state. Therefore, the consequence is to assume that the numerator is small. The result is attributable to the domain structure formation and its resistivity property. The domain structure can be formed using the competition between the magnetic shape anisotropy $\boldsymbol{K}_S$ and the uniaxial magnetic anisotropy $\boldsymbol{K}_U$ directed perpendicular to $\boldsymbol{K}_S$ as schematically shown in Fig. 8. $\boldsymbol{K}_U$ is basically fixed when the interface or heterojunction is formed, whereas $\boldsymbol{K}_S$ is dependent on the wire shape. As the wire width becomes smaller, $\boldsymbol{K}_S$ becomes larger and the magnetization tends to align along the major axis of the wire owing to the strong shape anisotropy, resulting in an unstable 180° domain structure and magnetization that tends to tilt, as shown in Fig. 8, because the projection component of the magnetic anisotropy in the minor axis direction of the wire is the origin of domain structure formation. Consequently, the MR ratio difference decreases with decreasing wire width as shown in Fig. 7. The result is one of the causes of the data fitting discrepancy seen in the narrow areas in Fig. 9. The other reason is that the domain wall width is not considered in the fitting curve, and the number of domains is estimated to be large, yielding the discrepancy.

In the discussion, we reconsider the contribution of the domain wall resistance. As shown in Fig. 4, the difference between the MR behaviors of the cases [1] $I \parallel H_{ext}$ & $I \perp H_A$ and [2] $I \perp H_{ext}$ in the presence of the stripe domain structure is clearly seen. The difference increases with the wire width. To explain the giant MR (GMR) effect, Valet and Fert described the transport properties of current perpendicular to the plane (CPP) multilayers by starting with a Boltzmann equation.[42] They took the spin diffusion length into account and also included both volume and interface spin-dependent scattering. Their model is very helpful for understanding the physical process in the CPP-GMR effect. The theoretical and experimental

reports demonstrate that the MR is inversely proportional to the ferromagnetic layer thickness. However, the description cannot be applied as it is suitable in the GMR effect because the corresponding ferromagnetic layer thickness and domain length in this study are much larger than the assumed spin relaxation length. Thus, the relatively large MR response observed in transport measurements alludes to the possibility that the spin-dependent scattering mechanism in domains and domain walls occurs.[40,43–48] The heterojunction structure composed of ferromagnetic and ferroelectric layers provides a crucial key to investigating the fundamental physical mechanism and producing artificial multiferroic functional materials and devices.

According to the theory of Levy and Zhang,[44] the domain wall resistivity arises from the mixture of resistivities in two spin channels. Here, $\beta$ is defined as $\beta = \rho_0^{\uparrow} / \rho_0^{\downarrow}$, where $\rho_0^{\uparrow}$ and $\rho_0^{\downarrow}$ denote the spin-up and spin-down channels, respectively. For current-in-wall (CIW) and current-perpendicular-to-wall (CPW) geometries, each resistivity ratio is described by the following formula:

$$\frac{\Delta\rho_{CIP}}{\rho_0} = \frac{\xi^2}{5}\frac{(\beta-1)^2}{\beta}, \tag{1}$$

$$\frac{\Delta\rho_{CPW}}{\rho_0} = \frac{\xi^2}{5}\frac{(\beta-1)^2}{\beta}\left(3+\frac{10\sqrt{\beta}}{\beta+1}\right), \tag{2}$$

where $\xi = \pi\hbar^2 k_F / 4mJ\delta_{DW}$, with $\hbar$, $k_F$, $m$, and $J$ being the Planck constant divided by $2\pi$, the Fermi wave velocity, the electron mass, and exchange splitting, respectively. The domain wall width $\delta_{DW}$ is given by

$$\delta_{DW} = \pi\sqrt{\frac{A}{K}}, \tag{3}$$

where $A$ and $K$ are the exchange stiffness constant and magnetic anisotropy energy, respectively.

$$\frac{\Delta\rho_{CPW}}{\rho_0} \propto \frac{1}{\delta_{DW}} \propto K \tag{4}$$

We note that the resistivity ratio described in Eqs. (1)−(3) is inversely proportional to $\delta_{DW}$ and proportional to the magnetic anisotropy. This means that the resistivity ratio is inversely proportional to $\delta_{DW}$ or is proportional to $K$ in the presence of domain walls. In our system, the whole magnetic anisotropy of the system is composed of $\boldsymbol{K}_S$ and $\boldsymbol{K}_U$ induced by the heterojunction. Considering the stripe domain formation case, since the magnetic anisotropic directions are orthogonal, we should consider the total effective magnetic anisotropy $K$ for the domain wall stability, which is determined by the balance between the shape magnetic and uniaxial magnetic anisotropies induced by the heterojunction. The projection component

Table 1
Relationships among $w$, $\boldsymbol{K}_S$, $\boldsymbol{K}_U$, $K$, and $\delta_{DW}$.

| | | | |
|---|---|---|---|
| Wire width, $w$ | narrow | → | wide |
| $\boldsymbol{K}_S$ | large | → | small |
| $\boldsymbol{K}_U$ | constant | → | constant |
| $K$ | small | → | large |
| $\delta_{DW}$ | large | → | small |

$K$ of the total magnetic anisotropy $\boldsymbol{K}_U + \boldsymbol{K}_S$ to the minor axis of the wire is the origin of the formed stripe domain structure. As shown in Fig. 8, the projection component is $\boldsymbol{K}_U$. Here, $\boldsymbol{K}_U$ is uniformly applied along the $X$-direction of the $LiNbO_3$ substrate, that is, $\boldsymbol{K}_U$ is constant. In this study, the length and thickness of the Ni wires are fixed. The wire width $w$ plays a significant role in varying $\boldsymbol{K}_S$. As $w$ increases, $\boldsymbol{K}_S$ decreases.[49] Then, $K$ increases with $w$. The relationships associated with $w$, $\boldsymbol{K}_S$, $\boldsymbol{K}_U$, $K$, and $\delta_{DW}$ are shown in Table 1.

As shown in Fig. 8, we found that the domain wall width decreases with increasing wire width. The MR ratio difference behavior, which increases with the wire width, between cases [1] and [2] in Fig. 4 suggests that the domain wall resistance might contribute the MR ratio difference.

## 5. Conclusions

The relatively large MR responses of Ni wires fabricated on single-crystal lithium niobate $LiNbO_3$ are measured at room temperature. In particular, we found that the MR characteristics are significantly dependent on the wire alignment and direction of an external magnetic field. The MR behaviors originate from the internal domain structure. The stripe domain or single-domain structure can be formed by controlling the wire alignment to the $X$-axis of $LiNbO_3$. The competition between the magnetic shape anisotropy and the uniaxial magnetic anisotropy derived from the heterojunction plays a significant role in controlling the domain structure. The heterojunction between the Ni layer and the $LiNbO_3$ substrate can induce the uniaxial magnetic anisotropy directed parallel to the $X$-axis of the $LiNbO_3$ substrate, while the uniaxial magnetic anisotropy is not induced in the Ni layer deposited on the $SiO_2$/Si substrate. The heterojunction between the Ni layer and the $LiNbO_3$ substrate enables the formation of the stripe domain structure in Ni wires with various widths. The difference in MR ratio increases with the wire width. The width dependence of the MR ratio difference with the formation of the stripe domain structure can be qualitatively explained using the series resistor circuit model. The discrepancy between the fitting and experimental data is considered to be the possible contribution of the domain wall resistance. This issue might be controversial for further study. Our multiferroic system with the heterojunction might provide a clue to investigating the essential domain wall resistivity. Finally, this investigation demonstrated that the MR could be enhanced by the formation of a stripe domain. This significant increase in MR ratio sheds light on developing sensor applications using an artificial multiferroic system.

## Acknowledgments

We thank Professor M. Shima of Gifu University for the measurement of magnetization hysteresis loops by VSM at Gifu University, Japan. This work was supported in part by JSPS Grants-in-Aid for Scientific Research B (No. 17H02755), JSPS Grants-in-Aid for Scientific Research C (No. 19K03757), JSPS Grants-in-Aid for Young Scientists A (No. 17H04795), and the Iketani Science and Technology Foundation. The experiments at the BL25SU and BL17SU beamlines of SPring-8 were performed with the approval and support of the Japan Synchrotron Radiation Research Institute (JASRI, Proposal Nos. 2013B1735, 2014B1398, 2016A1252, and 2016B1305).

## References

1 B. Hillebrands and K. E. Ounadiela, Eds.: Spin Dynamics in Confined Magnetic Structures (Springer, Berlin, 2002) Vols. I–III.
2 T. Schrefl, J. Fidler, K. J. Kirk, and J. N. Chapman: J. Magn. Magn. Mater. **175** (1997) 193.
3 K. Shigeto, T. Shinjo, and T. Ono: Appl. Phys. Lett. **75** (1999) 2815.
4 R. P. Cowburn, S. J. Gray, J. Ferré, J. A. C. Bland, and J. Miltat: J. Appl. Phys. **78** (1995) 7210.
5 T. Ono, H. Miyajima, K. Shigeto, K. Mibu, N. Hosoito, and T. Shinjo: Science **284** (1999) 468.
6 D. Atkinson, D. A. Allwood, G. Xiong, M. D. Cooke, C. C. Faulker, and R. P. Cowburn: Nat. Mater. **2** (2003) 85.
7 Y. Nakatani, A. Thiaville, and J. Miltat: Nat. Mater. **2** (2003) 521.
8 Y. Kasatani, A. Yamaguchi, H. Yamamoto, and H. Miyajima: Phys. Rev. B **81** (2010) 224425.
9 T. Shinjo, T. Okuno, R. Hassdorf, K. Shigeto, and T. Ono: Science **289** (2000) 930.
10 K. Yu. Guslienko, W. Scholz, R. W. Chantrell, and V. Novosad: Phys. Rev. B **71** (2005) 144407.
11 S.-B. Choe, Y. Acremann, A. Scholl, A. Bauer, A. Doran, J. Stöhr, and H. A. Padmore: Science **304** (2004) 420.
12 K. Yamada, S. Kasai, Y. Nakatani, K. Kobayashi, H. Kohno, A. Thiaville, and T. Ono: Nat. Mater. **6** (2007) 270.
13 M. Goto, H. Hata, A. Yamaguchi, Y. Nakatani, T. Yamaoka, Y. Nozaki, and H. Miyajima: Phys. Rev. B **84** (2011) 064406.
14 P. E. Roy, J. H. Lee, T. Trypiniotis, D. Anderson, G. A. C. Jones, D. Tse, and C. H. W. Barnes: Phys. Rev. B **79** (2009) 060407(R).
15 P. Grünberg, R. Schreiber, Y. Pand, M. B. Brodsky, and H. Soweres: Phys. Rev. Lett. **57** (1986) 2442.
16 M. N. Baibich, J. M. Broto, A. Fert, F. Nguyen Van Dau, F. Petroff, P. Etienne, G. Creuset, A. Friederich, and J. Chazelas: Phys. Rev. Lett. **61** (1988) 2472.
17 S. S. P. Parkin, R. Bhafra, and K. P. Roche: Phys. Rev. Lett. **66** (1991) 2152.
18 W. R. Bennett, W. Schwarzacher, and W. F. Egelhoff, Jr.: Phys. Rev. Lett. **65** (1990) 3169.
19 M. T. Johnson, S. T. Purcell, N. W. E. McGee, R. Coehoorm, J. aan de Stegge, and W. Hoving: Phys. Rev. Lett. **68** (1992) 2688.
20 D. Halley, O. Bengone, S. Boukari, and W. Weber: Phys. Rev. Lett. **102** (2009) 027201.
21 P. Bruno: Phys. Rev. B **52** (1995) 411.
22 A. Yamaguchi, T. Kishimoto, and H. Miyajima: Appl. Phys. Express **3** (2010) 093004.
23 A. Yamaguchi, T. Ohkouchi, A. Yasui, T. Kinoshita, and K. Yamada: IEEE Trans. Magn. **53** (2017) 8108504.
24 A. Yamaguchi, T. Ohkouchi, A. Yasui, T. Kinoshita, and K. Yamada: J. Magn. Magn. Mater. **453** (2018) 107.
25 A. Yamaguchi, H. Hata, M. Goto, M. Kodama, Y. Kasatani, K. Sekiguchi, Y. Nozaki, T. Ohkochi, M. Kotsugi, and T. Kinoshita: Jpn. J. Appl. Phys. **55** (2016) 023002.
26 A. Barman, V. V. Kruglyak, R. J. Hicken, J. M. Rowe, A. Kundrotaite, J. Scott, and M. Rahman: Phys. Rev. B **69** (2004) 174426.
27 T. Ogasawara: Jpn. J. Appl. Phys. **56** (2017) 108002.
28 C. Bayer, S. O. Demokritov, B. Hillebrands, and A. N. Slavin: Appl. Phys. Lett. **82** (2003) 607.
29 A. Ercole, A. O. Adeyeye, J. A. C. Bland, and D. G. Hasko: Phys. Rev. B **58** (1998) 345.

30 A. A. Tulapurkar, Y. Suzuki, A. Fukushima, H. Kubota, H. Maehara, K. Tsunekawa, D. D. Djayaprawira, N. Watanabe, and S. Yuasa: Nature **438** (2005) 339.
31 J. C. Sankey, P. M. Braganca, A. G. F. Garcia, I. N. Krivorotov, R. A. Buhrman, and D. C. Ralph: Phys. Rev. Lett. **96** (2006) 227601.
32 A. Yamaguchi, H. Miyajima, T. Ono, Y. Suzuki, and S. Yuasa: Appl. Phys. Lett. **90** (2007) 182507.
33 A. Yamaguchi, A. Nakao, T. Ohkouchi, A. Yasui, T. Kinoshita, Y. Utsumi, T. Saiki, and K. Yamada: AIP Adv. **8** (2018) 056411.
34 A. Yamaguchi, K. Motoi, A. Hirohata, H. Miyajima, Y. Miyashita, and Y. Sanada: Phys. Rev. B **78** (2008) 104401.
35 M. Fiebig, Th. Lottermoser, D. Meier, and M. Trassin: Nat. Rev. Mater. **1** (2016) 16046.
36 J. Dean, M. T. Bryan, J. D. Cooper, A. Virbule, J. E. Cunningham, and T. J. Hayward: Appl. Phys. Lett. 107 (2015) 142405.
37 T. A. Ostler, R. Cuadrado, R. W. Chantrell, A. W. Rushforth, and S. A. Cavill: Phys. Rev. Lett. **115** (2015) 067202.
38 L. E. Dzyaloshinskii: Sov. Phys., JIETP **5** (1957) 1259.
39 T. Moriya: Phys. Rev. **120** (1960) 91.
40 Y. Yin, D.-S. Han, J.-S. Kim, R. Lavrijsen, K.-J. Lee, S.-W. Lee, K.-W. Kim, H.-W. Lee, H. J. M. Swagten, and B. Koopmans: Appl. Phys. Lett. **110** (2017) 122401.
41 Y. Nakatani, Y. Uesaka, and N. Hayashi: Jpn. J. Appl. Phys. **28** (1989) 2485.
42 T. Valet and A. Fert: Phys. Rev. B **48** (1993) 7099.
43 U. Rüdiger, J. Yu, L. Thomas, S. S. P. Parkin, and A. D. Kent: Phys. Rev. B **59** (1999) 11914.
44 P. M. Levy and S. Zhang: Phys. Rev. Lett. **70** (1997) 5110.
45 G. Tatara and H. Fukuyama: Phys. Rev. Lett. **78** (1997) 3773.
46 H. Tanigawa, A. Yamaguchi, S. Kasai, T. Ono, T. Seki, T. Shima, and K. Takanashi: J. Appl. Phys. **99** (2006) 08G520.
47 W. Chen, L. Qian, and G. Xiao: Phys. Rev. B **98** (2018) 174402.
48 Y. Ishikuro, M. Kawaguchi, Y.-C. Lau, Y. Nakatani, and M. Hayashi: Appl. Phys. Express **11** (2018) 073001.
49 A. Aharoni: J. Appl. Phys. **83** (1998) 3432.